Materials Today 92 (2026) 160–172

Contents lists available at ScienceDirect

Materials Today

journal homepage: www.elsevier.com/locate/mattod

Shining under stress: hybrid coordination polymer as a multifunctional solution for mechanoluminochromic materials

E. Contini [a,b], L. Contini [a], L. Gatti [a,b], F. Mongioì [c,e], D. Fazzi [a,b], T.M. Brugo [c,d,e], D. Genovese [a,b], L. Maini [a,b], C. Gualandi [a,b,d,*]

[a] Department of Chemistry "G. Ciamician", University of Bologna, via Gobetti 85, 40129 Bologna, Italy
[b] INSTM UdR of Bologna, University of Bologna, via Gobetti 85, 40129 Bologna, Italy
[c] Department of Industrial Engineering, University of Bologna, Viale Risorgimento 2, 40136 Bologna, Italy
[d] Interdepartmental Center for Industrial Research on Advanced Applications in Mechanical Engineering and Materials Technology, CIRI-MAM, University of Bologna, Viale Risorgimento, 2, Bologna 40136, Italy
[e] INSTM UdR of Bologna, University of Bologna, Viale Risorgimento 2, 40136 Bologna, Italy

ARTICLE INFO

Keywords:
Mechanoluminochromic polymers
Mechanochromism
Stress sensing
Hybrid coordination polymers
Smart materials

ABSTRACT

Mechanochromic materials are studied as optical probes for mechanical stress in self-diagnostic devices. They rely on mechanoresponsive components undergoing structural changes (e.g. bond cleavage, conformational change, supramolecular rearrangement) upon application of a mechanical force. Depending on the active component, the state-of-the-art approaches face significant limitations: scarce optical changes, difficulty in detecting low stresses and deformation, response limited to specific deformation modes, and some lack scalability. This study proposes the use of mechanoluminochromic copper (I) iodide-based hybrid coordination polymers as a scalable and universal solution to achieve mechanoluminochromism across various polymer types and sensitivity to all deformation modes. $[(CuI)3\text{-}Br\text{-}py]_n$ is used as additive for developing highly sensitive mechanoluminochromic polymeric materials responding to both in-plane and out-of-plane mechanical stresses, including tensile, compression, impact, and scratching. The strong and persistent mechanoluminochromic response is found to linearly correlate to the strain (under tensile deformation) and to the force (under impact), independent from the additive concentration, and tunable by the polymer matrix features.

Introduction

Monitoring the impact of mechanical stresses on the integrity of polymer-based materials and devices is crucial for preventing structural failure. Mechanochromic polymers, whose optical properties change with mechanical stress, offer a promising solution to this challenge [1–3]. Current mechanochromic polymers primarily rely on incorporating chromogenic units (often called "mechanophores") in polymeric matrices that feature strong variations of their optical properties upon mechanical stress. These chromophores are characterized by either a cleavable covalent bond or intermolecular interactions that affect their optical properties when modified. Among the possible optical variations, changes in the emission spectrum, occurring in ratiometric mechanoluminochromic (MLC) materials, are desirable owing to the sensitivity of luminescence (as compared to absorbance), and to the absolute nature of ratiometric intensity [4–16].

However, state-of-the-art approaches present significant drawbacks: covalent inclusion of mechanophores often requires lengthy synthesis [17–24], whereas physical dispersion of mechanophores is subject to time and temperature-dependent aggregation, thus making the MLC response scarcely controllable. Moreover, for both approaches, the response is often observed only with tensile stresses [9,25–28]. Additionally, since both approaches rely on bond/interaction ruptures, high stresses/strains are often required to obtain a detectable response, limiting their practical application [3,20–22,29–32].

Here, we propose the use of hybrid coordination polymers (HCPs) as additives in polymeric matrices, representing a new approach for obtaining MLC materials characterized by a high sensitivity and reproducibility to various types of mechanical stresses (i.e., tensile, compression, impact and scratch), in a broad range of conditions and forces. In particular, copper (I) halide-based hybrid coordination polymers (CuX-based HCPs) offer several advantages, like diverse structures,

* Corresponding author.
E-mail address: c.gualandi@unibo.it (C. Gualandi).

https://doi.org/10.1016/j.mattod.2025.11.034
Received 4 September 2025; Received in revised form 10 October 2025; Accepted 29 November 2025
Available online 6 December 2025

environmental stability, ease of synthesis, and tunable photophysical properties [33–47]. In addition, compared to other mechanoresponsive compounds based on noble and rare earth metals [16], Cu-based HCPs are less toxic and cheaper, with their precursors being more abundant in nature. These materials exhibit intriguing mechanoluminochromic behavior caused by stress-induced alterations of bond lengths [35,48–50]. These optical and stimuli-responsive properties make HCPs promising for developing industrially scalable additive-based MLC materials [33]. In addition, since the mechanism behind their mechanoluminocromism is based on small bond-length alterations, HCPs are not expected to suffer flaws typical of additive-based MLC materials, such as time-dependent response and high strain response threshold [41].

Results and discussion

HCP mechanoluminochromism

$[(CuI)3\text{-}Br\text{-}py]_n$ (Fig. 1a), firstly synthesized by S. Masahara et al. [51], was chosen for our investigation because of its structural features, namely a double $[Cu_2I_2]$ chain and the presence of unsupported cuprofilic interactions [52], which are crucial for the mechanochromism of this family of materials [33]. Furthermore, its colorless nature makes it a versatile filler for applications in the realm of mechanoluminochromic coatings and polymer masterbatches without affecting aestethic properties. Albeit two polymorphs of $[(CuI)3\text{-}Br\text{-}py]_n$ are currently deposited in the Cambridge Structural Database (CSD), one with an orthorhombic [51] and one with a monoclinic [53] lattice, all synthetic conditions employed in this work reproducibly yielded the orthorhombic phase. The compound has been synthesized both as single crystal, through triple-layer crystallization, and as polycrystalline powder via slurry (Fig. S1 and Table S1). The phase nature of the bulk powder product and its purity were confirmed by comparison of the experimental powder diffraction pattern (PXRD) with the one calculated based on its single crystal structure (Fig. S2). The particle dimensions distribution was also assessed via scanning electron microscopy (SEM) (Fig. 1b(i), 1b(ii), Fig. S3, and Fig. S4). Particles were found to be needle-shaped, with a long axis (L) of roughly 3 μm and a diameter (∅) below 2 μm.

The powder was ground in a Retsch MM200 ball mill for 5 min at 25 Hz to probe the material response to shear and impact forces. Interestingly, no new peaks emerged in the PXRD pattern of the ground sample (Fig. 1c), indicating that no change in the crystalline form occurred. Moreover, the background remained unchanged, indicating no amorphization. However, peak broadening was observed in the ground sample, indicating a modification in the microstructure of the crystals induced by grinding. Such a change was studied by modelling the distribution of spherical crystallite domains using Rietveld refinement and whole powder pattern modeling (WPPM) analysis [54]. These results proved that a decrease in crystallite domain size (D) occurred after grinding (166.2 ± 0.8 for the pristine powder and 15.80 ± 0.03 after grinding), with an overall shift of the lognormal distribution profile towards lower D values (Fig. 1d and Table S2). This result was mirrored by a decrease in particle dimensions and a loss of needle-like morphology observed through SEM micrographs (Fig. 1b(iii) and 1b (iv)).

Images captured under UV irradiation (λ_{ex} at 365 nm) showcased a striking MLC response (Fig. 1e), shifting the emission color from blue to green upon grinding. This drastic emission color change was mirrored in the solid-state emission spectra, shifting from a maximum at 440 nm (pristine material) to 505 nm (ground). The mechanoluminochromism observed in CuI-based HCP has been ascribed in literature to the presence of two triplet emitting states located at high (HE) and low energy (LE), respectively, whose populations is very sensitive to the Cu-Cu interatomic separation. It has thus been hypothesized that defects introduced upon grinding, such as dislocations, stacking faults, and vacancies, can cause a shortening of the Cu-Cu distances [33,37,47], inducing a change in the emission from the HE to the LE state, resulting in a red-shift [55].

The perceived color under white light remained essentially unchanged (Fig. S5), indicating that grinding did not significantly alter the absorption properties. Notably, having a response solely in emission offers significant advantages compared to the absorption-based counterpart, such as no alteration of the aesthetic appearance of the material and highly sensitive detection.

The mechanoluminochromism was further investigated using confocal microscopy by analyzing single crystals of $[(CuI)3\text{-}Br\text{-}py]_n$ before and after the introduction of localized mechanical damages with a metal spatula (Fig. S6). Images reported in Fig. S6b show how damaged crystals display green emission only in the fractured region (i.e., the part affected mainly by defects), whereas the remaining crystal still displays blue emission.

The powder emission was measured real-time during grinding to investigate the MLC response of $[(CuI)3\text{-}Br\text{-}py]_n$ under shear stresses (Fig. S7 and Video S1). A key aspect of this experiment involved monitoring the ratiometric emission intensity between the green (I_{Green} at 505 nm) and blue (I_{Blue} at 440 nm) emission as a function of the grinding time (Fig. 1f). As the grinding started, the powder was uniformly spread on the plate (as shown in the 5 s image of Fig. 1f). Notably, the I_{Green}/I_{Blue} ratio rapidly increased linearly in the first 20 s, indicating an instantaneous MLC response upon shear stress application. A plateau followed, indicating a maximum attainable enhancement in I_{Green}/I_{Blue} of approximately 300 % under these deformation conditions. This real-time analysis underscores the remarkably fast $[(CuI)3\text{-}Br\text{-}py]_n$ mechanoluminochromism, demonstrating its potential for applications demanding immediate response under mechanical stimuli.

Recrystallization experiments were conducted on the ground powder to assess the recyclability of the fillers by testing the reversibility of the MLC response. Specifically, the mechanically damaged powder was exposed to acetonitrile (MeCN) vapors for 48 h. After this treatment, the initial blue emission was recovered (Figs. 2a and b), the morphology of the crystals was almost completely restored (Fig. 2c, Fig. S2-S3, S8-S9), and the recycled powder retained the MLC response (Figs. 2a and b). PXRD patterns (Fig. S10) proved that no phase change occurred during these grinding-recrystallization cycles. Variation in domain size distributions were studied and no significant differences were observed when comparing the lognormal domain size distribution curves of the ground and reground powder (Fig. S11, Table S2 and S3), highlighting the recyclability of the compound. To further assess the chromophore recyclability, four sequential recrystallization-grinding cycles were carried out (Fig. S12). The consistent recovery of the emission and mechanochromic properties after each recycling confirmed the material reversibility and resilience to repeated grinding and recrystallization.

Mechanoluminochromic response of PVAc/HCP composites

Two MLC materials were prepared using a polyvinyl acetate (PVAc) matrix and different amounts of $[(CuI)3\text{-}Br\text{-}py]_n$ filler (named 5 wt% and 10 wt%, based on the filler content). PVAc was chosen for composite preparation due to its typical thermoplastic behavior and high toughness, allowing testing of the composites under different types of mechanical loads before sample failure.

The preparation method is detailed in the Experimental Section and depicted in Fig. 3a. PXRD and thermogravimetric analysis (TGA) confirmed that processing did not alter the filler crystal structure (Fig. S13 and S14) and that the filler content matched the intended composition (Table S4). Differential scanning calorimetry (DSC) analysis examined the thermal transitions of the composites, demonstrating that the filler slightly increased the glass transition temperature (T_g) compared to the pure polymer (Fig. S15 and Table S5). This variation in the T_g is also evident in the mechanical behavior of the composites, exhibiting improved rigidity compared to the polymeric matrix, with higher Young's modulus and lower deformation at break (Fig. S16 and

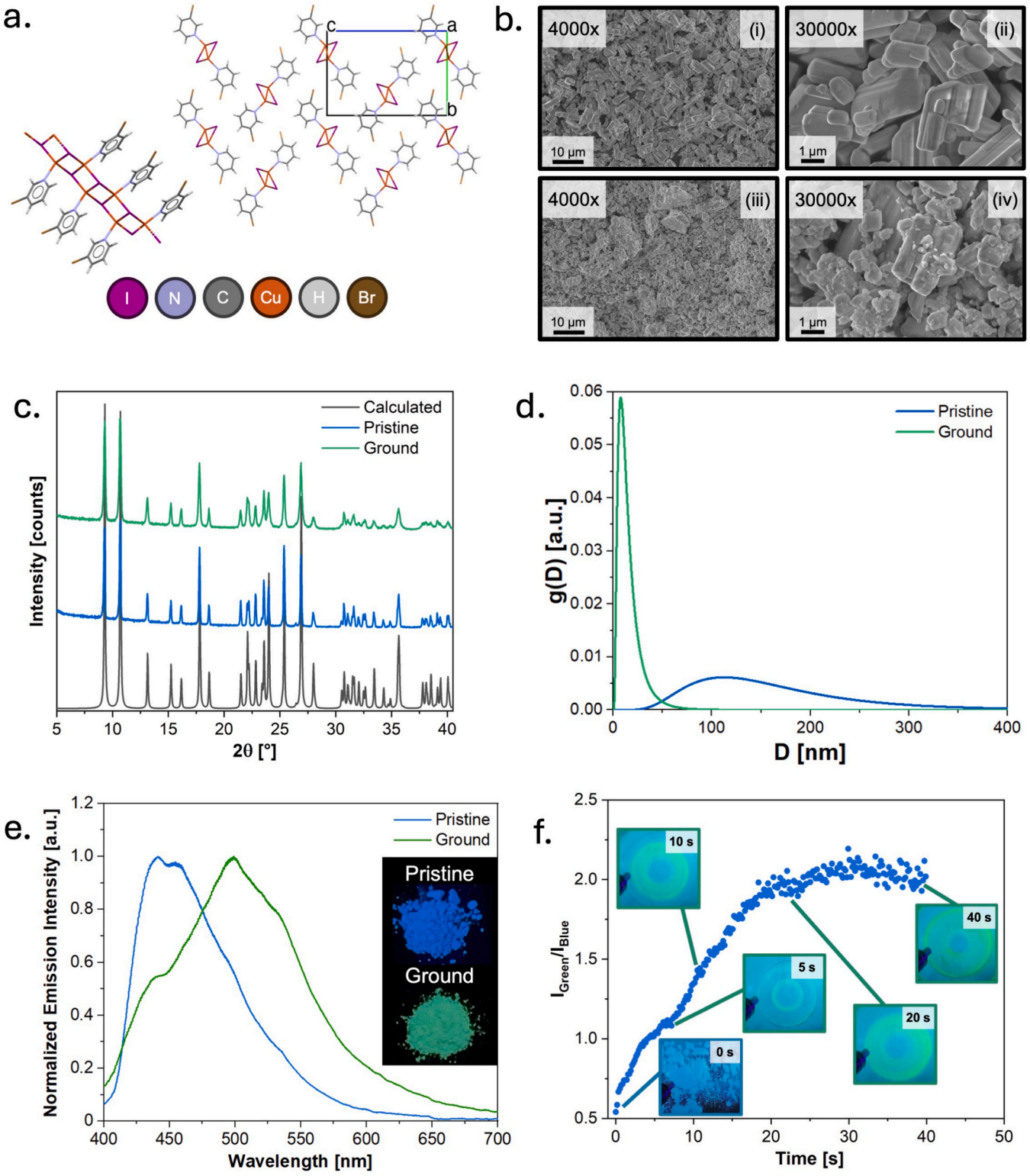

Fig. 1. a) quasi-1d structure of an individual chain of $[(CuI)3\text{-}Br\text{-}py]_n$ (left), crystalline packing of $[(CuI)3\text{-}Br\text{-}py]_n$ chains viewed along the a-axis (right); b) SEM micrograph images of pristine (i, ii) and ground $[(CuI)3\text{-}Br\text{-}py]_n$ (5 min at 25 Hz) (iii, iv); c) X-ray powder patterns of pristine (blue), ground (green) and calculated (grey) $[(CuI)3\text{-}Br\text{-}py]_n$; d) Lognormal crystallite domain size distribution of pristine (blue) and ground (green) $[(CuI)3\text{-}Br\text{-}py]_n$ determined by WPPM analysis; e) solid-state emission spectra of pristine (blue) and ground (green) $[(CuI)3\text{-}Br\text{-}py]_n$ and corresponding images under UV-light (λ_{ex} at 365 nm); f) I_{Green}/I_{Blue} vs. time during real-time grinding of $[(CuI)3\text{-}Br\text{-}py]_n$ inset shows images under UV light collected during the experiment.

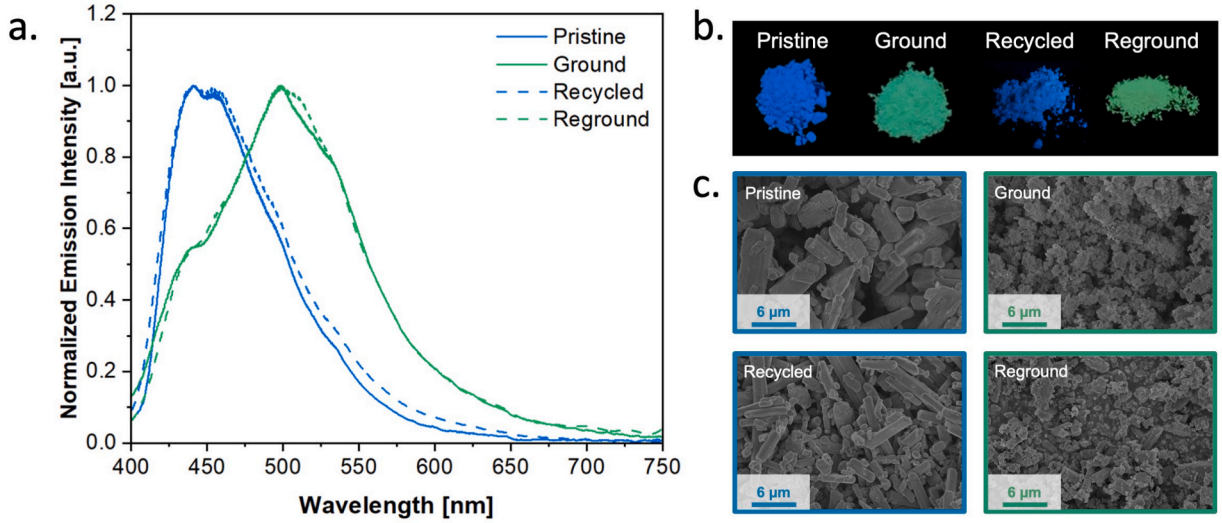

Fig. 2. a) solid-state emission spectra of pristine (blue) and ground (green) $[(CuI)3\text{-}Br\text{-}py]_n$ before recycling (line) and after recycling (dash); b) images under UV-light (λ_{ex} at 365 nm) of pristine, ground, recycled and reground $[(CuI)3\text{-}Br\text{-}py]_n$; c) SEM micrograph images of pristine, ground, recycled and reground $[(CuI)3\text{-}Br\text{-}py]_n$ at 10000x magnification.

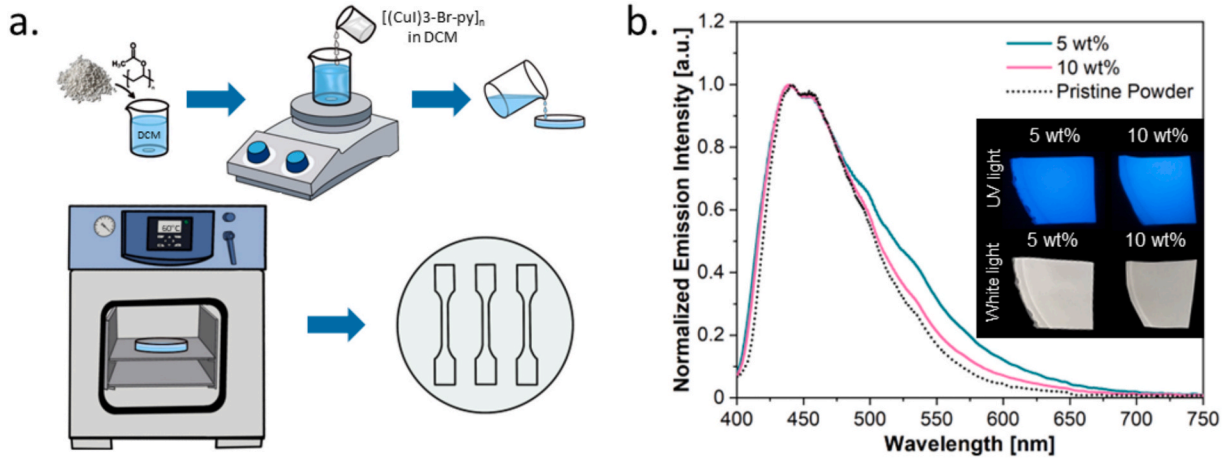

Fig. 3. a) schematic representation of composite preparation that includes: dissolution of the polymer indichloromethane (DCM), addition of $[(CuI)3\text{-}Br\text{-}py]_n$ to the polymeric solution, casting of the obtained suspension, and dying in oven at 60 °C for 48 h; b) solid-state emission spectra of 5 wt% composite (teal), 10 wt% composite (fuchsia), and pristine $[(CuI)3\text{-}Br\text{-}py]_n$ powder (black short dot); images of composites with 5 wt% and 10 wt% $[(CuI)3\text{-}Br\text{-}py]_n$ under UV-light (λ_{ex} at 365 nm) and white light.

Table S6). These observations, as well as SEM micrographs of the composite section (Fig. S17), suggest good adhesion between the filler and the matrix [56–58].

The emission spectra and pictures under UV light of the composites (Fig. 3b) confirmed that the processing and the inclusion in the PVAc matrix did not alter the emission properties of the HCP. Indeed, the spectra of the composites were nearly identical to that of the pristine powder, with a minor green emission enhancement in the 5 wt% composite. This difference likely arises from limited damage introduced to the crystals during material preparation.

After assessing that the properties of the filler were retained in the composite, the MLC response of the composites was evaluated under various mechanical stimuli, namely tensile, compression, and low-velocity impact.

The MLC response was recorded in real-time during tensile stress–-strain experiments for 5 wt% and 10 wt% composites (Fig. 4a). Since PVAc displays a high strain-rate dependency, becoming stiffer at higher strain rates (Fig. S16 and Table S6), the composites were tested at two different strain rates to assess how this parameter affected the MLC behavoiur.

Under UV light, all tested samples showed a blue-to-green shift in emission (Fig. 4a), while white light images showed minimal variations, confirming that the optical response primarily regards only the emission signal. Emission spectra acquired in real-time during tensile tests of 5 wt % (Figs. 4c and 4d) and 10 wt% samples (Figs. S18) confirmed a red shift in the emission with increasing strain (Video S2, Video S3).

To quantify the MLC response, the emission intensity ratio I_{Green}/I_{Blue} was plotted as a function of strain (Fig. 4b). For all concentrations and strain rates, I_{Green}/I_{Blue} linearly increased in the range 0–75 % strain, then remained constant. This change of trend may be, at least in part, ascribed to the experimental set-up. Indeed, the optical fiber of the compacted spectrometer was fixed on the tensile machine frame while the specimen was pullet only on one direction. Thus, for high specimen elongations, the fiber optic pointed on a region close to the grip instead on its central part. Samples with different concentrations at the same strain rate showed comparable slopes in the 0–75 % strain region (Table S7). Conversely, significant differences emerged when comparing responses at different strain rates. At the highest tested strain rate, the

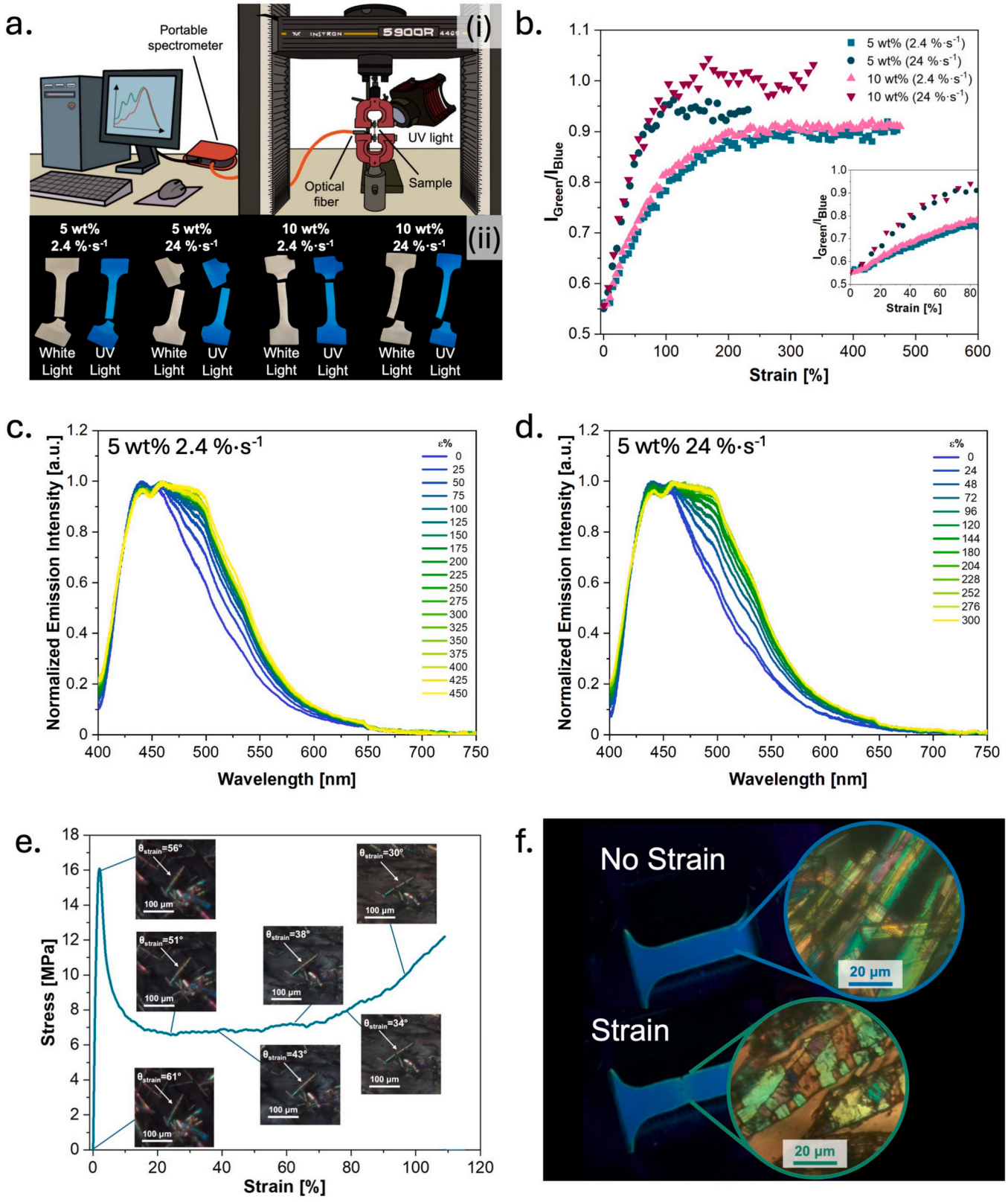

Fig. 4. A) schematic representation of the setup employed for the real-time tensile stress–strain MLC characterization, the sample emission spectra were acquired by exploiting a Thorlabs compact spectrometer coupled to a 365 nm LED lamp as the near-field probe (i); images under UV (λ_{ex} at 365 nm) and white light of 5 wt% and 10 wt% samples after break (ii); b) I_{Green}/I_{Blue} as a function of strain for 5 wt% composite deformed at 2.4 %·s^{-1} (light teal squares) and 24 %·s^{-1} (dark teal circles), 10 wt% composite deformed at 2.4 %·s^{-1} (fuchsia triangles) and 24 %·s^{-1} (dark fuchsia triangles); solid-state emission spectra at increasing strains of 5 wt% composite deformed with a crosshead speed of c) 2.4 %·s^{-1} and d) 24 %·s^{-1}; e) stress–strain curve of SC-2 wt% sample and POM images (5x) at selected strain with indication of the angle between the strain direction and the long-crystal axis; f) POM images (50x) under UV-light (λ_{ex} at 365 nm) of pristine and stretched SC-2 wt % sample.

linear response region displays the steepest slopes, resulting in an approximate 80 % increase in I_{Green}/I_{Blue}, substantially higher than ca. 65 % increase recorded for the samples deformed with a lower strain rate. Therefore, the MLC response reflects the strain-rate dependency of the PVAc matrix, suggesting a more efficient stress transfer from the matrix to the filler as the matrix's elastic modulus increases with increasing strain rate. Notably, samples were readily mechanoluminochromically responsive as soon as the deformation started, with no strain threshold for mechanoactivation (Fig. 4b, inset). These results stand out as a major innovation in MLC-based structural monitoring thanks to the instantaneous and sensitive response, which, in previously reported approaches, is typically achieved only at large deformations [3,7].

To shed light on the microscopic modifications that occur in the composite under tensile stress, a composite containing 2 wt% of $[(CuI)3\text{-}Br\text{-}py]_n$ single crystals (SC), named SC-2 wt% was prepared as described in the Experimental Section. These crystals are, in fact, larger compared to the polycrystalline powder counterpart used for the previous tests and can thus be easily identified under a polarized optical microscope (POM). The microscopic rearrangements of the crystals during tensile stress–strain test were followed in real time (Video S4). In the pristine sample, the crystals exhibited no significant preferential orientation (Fig. 4e and S19) and blue emission under UV light (Fig. 4f). However, right after the application of the stress, the crystals start to progressively align with the strain direction (Fig. 4e). At high strain, the crystals were mostly aligned, appeared fractured, and showed a noticeable MLC response under UV light (Fig. 4f and S19).

Following the intriguing strain-rate dependent mechanochromism

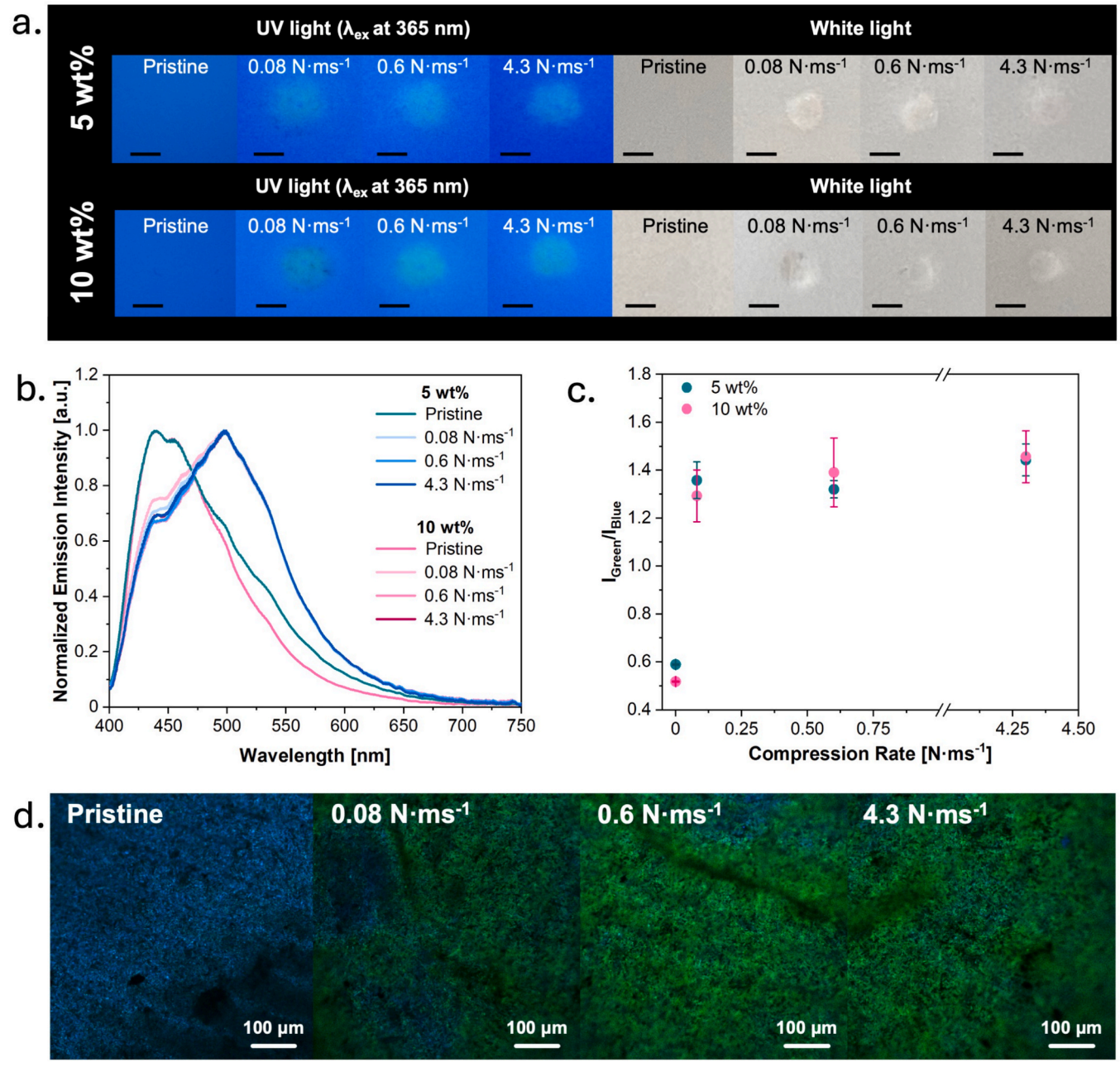

Fig. 5. a) images under UV (λ_{ex} at 365 nm) and white light of pristine 5 wt% and 10 wt% samples and after compression tests performed at various compression rates (scale bars = 2 mm); b) Solid-state emission spectra of pristine 5 wt% and 10 wt% samples and after compression tests performed at various compression rates; c) I_{Green}/I_{Blue} as a function of the compression rate for 5 wt% (teal) and 10 wt% (fuchsia) samples; d) confocal microscopy images of pristine and compressed 10 wt% samples (magnification: 20x, λ_{ex} at 401.9 nm, λ_{em} at 450 ± 25 nm and 525 ± 25 nm, objNA: 0.75, pixel size 1.25 µm·px^{-1}).

observed in tensile tests, the response of the composites to compression stresses was also explored. Compression tests were conducted up to a maximum force of 1500 N with varying compression rates (Fig. S20 and S21). Images under UV light (Fig. 5a) confirmed a distinct MLC response across all compression rates while no significant color changes under white light were observed.

Emission spectra (Fig. 5b) and confocal microscopy images (Fig. 5d) confirmed that compressed samples exhibit a red-shifted emission compared to pristine materials. The I_{Green}/I_{Blue} emission intensity ratio, plotted against compression rate (Fig. 5c), revealed no significant difference in samples bearing different filler concentrations, similar to what was observed in tensile stress–strain experiments. However, unlike the latter, the tested compression rates had no measurable influence on the MLC response, which depended only on the final compression force. This irreversible and rate-independent response under compression makes these composites highly attractive for impact damage monitoring applications.

Mechanoluminochromic characterization was thus performed after low-velocity impact (in the range c.a. 400–2200 $N{\cdot}ms^{-1}$) on both composites after impacts across a broad range of forces (Fig. S22 and S23a and S23b). As observed in compression experiments, after the application of impact forces, the emission spectra (reported in Fig. 6a and Fig. S24) revealed a strong red shift in emission, readily visible in the images of the impacted composites under UV light (Fig. 6b). Furthermore, ratiometric I_{Green}/I_{Blue} emission intensity plots displayed a linear relationship with the applied force for both concentrations (Fig. 6c and Table S8), incrementing the optical signal by ca. 300 % at the maximum tested force of 2800 N. To better assess the effect of the filler content, additional composites containing 2.5 wt% and 7.5 wt% of $[(CuI)3\text{-}Br\text{-}py]_n$ were tested under low-velocity impact across a broad range of forces (Fig. S23c and d). As for 5 and 10 wt% PVAc composites, the application of impact forces revealed a red shift in emission (Fig. S25 a and b) also visible under UV irradiation (Fig. S25c) and linearly correlated to the applied force (Fig. 6c and Table S8). As for tensile and compression experiments, also for low-velocity impacts the MLC response was found to be independent on the filler concentration.

Finally, confocal microscopy images of the impacted samples revealed that the mechanoluminochromic filler allows for high-resolution spatial mapping of the mechanical history of the composite, further highlighting its potential for damage assessment (Fig. 6d and Video S5). Interestingly, the evident presence of a blue-emissive region in the center of the impacted region (Video S5 and Fig. S26) indicates that the MLC response is the result of a combination of stress (i.e bending, compression, and shear) rather than just homogeneous (hydrostatic) pressure. This special feature is of exceptionally high value in materials designed for shockwave sensing and monitoring [59].

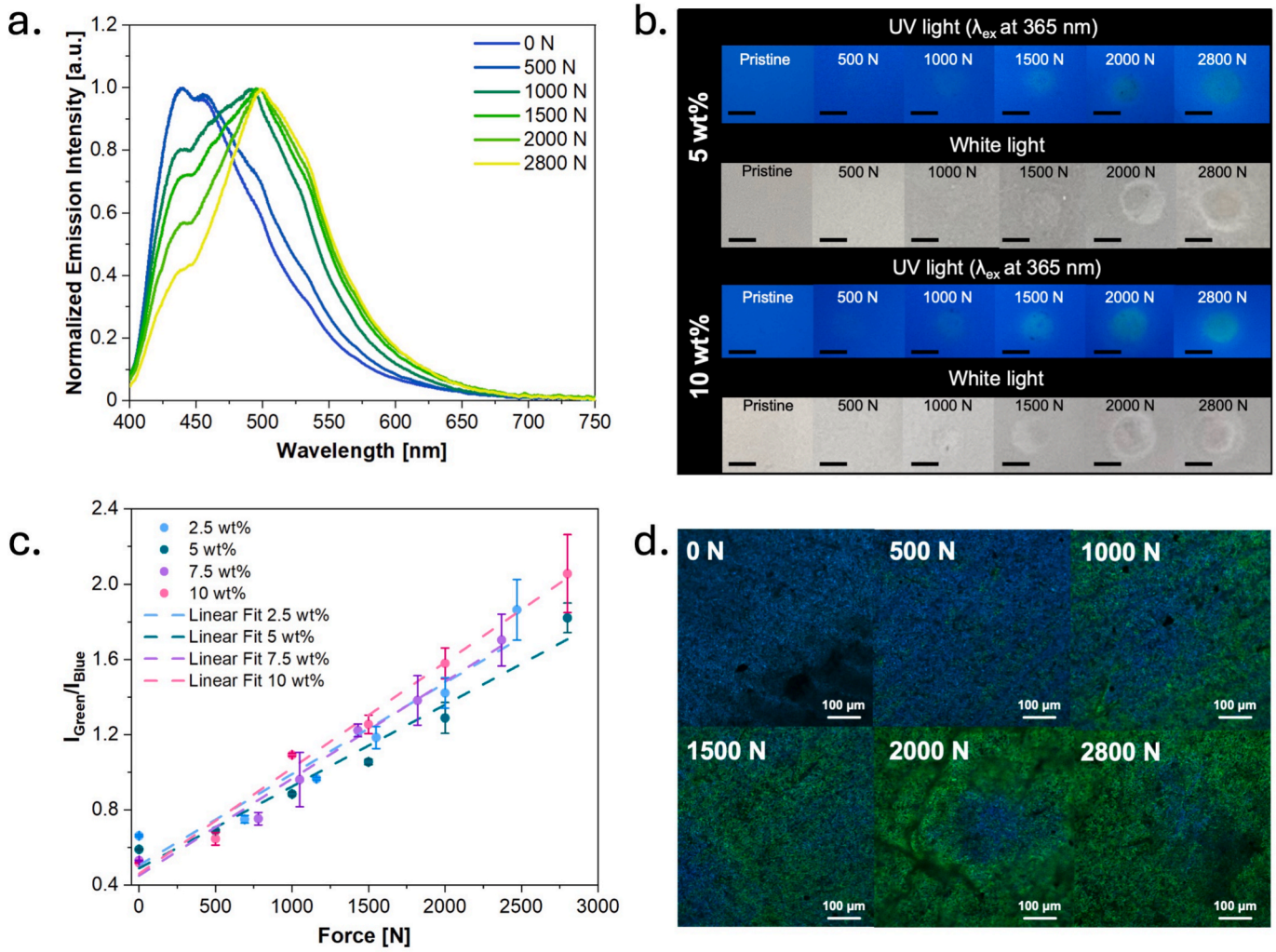

Fig. 6. a) solid-state emission spectra of pristine 5 wt% sample and after impact test at various forces; b) images under UV (λ_{ex} at 365 nm) and white light of pristine 5 wt% and 10 wt% samples and after impact test at various forces (scale bars = 2 mm); c) I_{Green}/I_{Blue} as a function of impact force for 2.5 wt% (light blue), 5 wt% (teal), 7.5 wt% (purple), and 10 wt% (fuchsia) samples; d) confocal microscopy images of pristine and impacted 10 wt% samples (magnification: 20x, λ_{ex} at 401.9 nm, λ_{em} at 450 ± 25 nm and 525 ± 25 nm, objNA: 0.75, pixel size 1.25 $\mu m{\cdot}px^{-1}$).

The PVAc/HCP composites also showed mechanochromism under scratching (Video S6) and bending (Video S7), demonstrating that these materials can sense any kind of mechanical deformation and highlighting, perspectively, the broad range of possible applications.

Emission spectra recorded six months following mechanical impact revealed no significant changes compared to those obtained immediately post-deformation (Fig. S27), underscoring the long-term stability of the MLC response. The persistency of the MLC response was further evaluated by subjecting PVAc 5 wt% samples impacted with a 2000 N force to sequential cooling to –10 °C and heating to 60 °C. As shown in

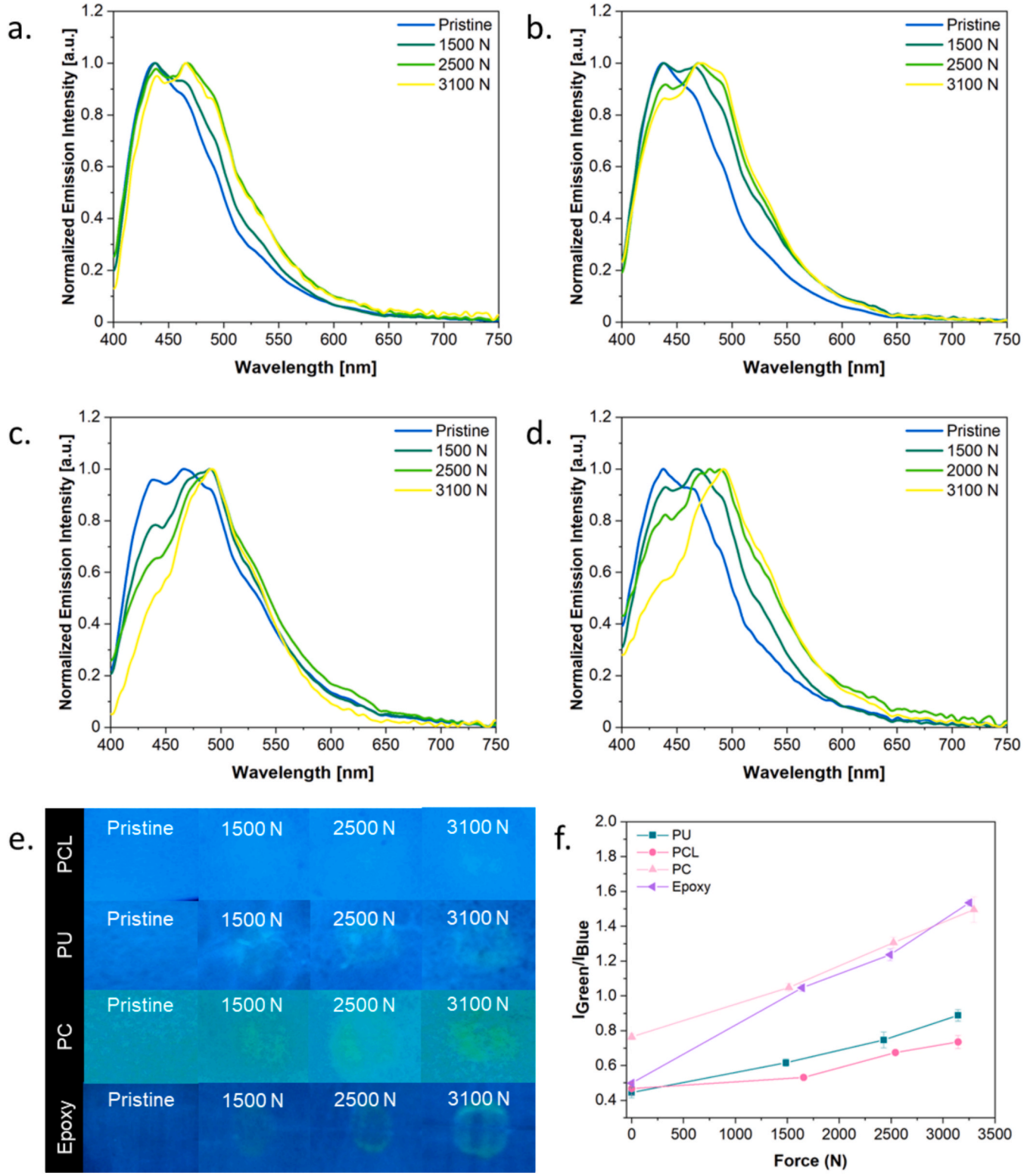

Fig. 7. Solid-state emission spectra of pristine and impacted composites containinig 5 wt% of $[(CuI)3\text{-}Br\text{-}py]_n$ dispersed in: a) PCL, b) PU, c) PC and d) Epoxy; e) images under UV (λ_{ex} at 365 nm) of pristine and impacted 5 wt% composites; f) I_{Green}/I_{Blue} as a function of the impact force for composites containinig 5 wt% of $[(CuI)3\text{-}Br\text{-}py]_n$ dispersed in PU (teal squares), PCL (fuchsia circles), PC (pink triangles), and Epoxy (purple triangles).

Fig. S28, the MLC response has some dependency on the temperature but upon returning the sample to room temperature, the response fully recovered, demonstrating the reversibility and persistence of the MLC behavior under thermal stimuli. We suggest that the reversible spectral changes observed upon varying the temperature are ascribable to slight and fully reversible lattice variations, in particular Cu-Cu separations, thus impacting both the energies and relative populations of the emissive excited states. Such mechanisms are currently under investigation and will be the subject of future works.

Additionally, the stability of the MLC response was tested under accelerated aging conditions by maintaining both pristine and impacted 5 wt% PVAc composites at 60 °C and 100 % relative humidity for 24 h. Comparison of the corresponding emission spectra and MLC response (Fig. S29) revealed that the response was preserved in the impacted samples, and no detectable changes occurred in the pristine material, further attesting the durability of the system under harsh environmental conditions.

Following the promising recyclability observed for the powdered material, the chemical recyclability of PVAc 5 wt% composite was also investigated. Scratched films were treated with acetonitrile using a cotton swab, as shown in Video S8. Remarkably, within one minute of application, the original blue emission was fully restored, and the scratch, clearly visible under UV irradiation prior to treatment, was no longer detectable. Notably, the MLC response of the film remained intact following this recycling process, indicating full functional recovery.

Role of the polymer matrix on the mechanoluminochromic response in HCP-based composites

The mechanoluminochromic response of PVAc/[(CuI)3-Br-py]$_n$ composites prompted further exploration of the MLC potential of [(CuI)3-Br-py]$_n$ as a versatile filler in various polymeric matrices. Polymers with different thermomechanical properties were selected to systematically evaluate the influence of the matrix properties on the MLC response. Specifically, these included a semicrystalline polymer with a low T_g (polycaprolactone, PCL), a thermoplastic elastomer (polyurethane, PU), an amorphous polymer with a high T_g (polycarbonate, PC), and a crosslinked epoxy-based resin with a high T_g (Fig. S30 and Table S9).

As described in the Experimental Section, all composites were prepared with a nominal [(CuI)3-Br-py]$_n$ content of 5 wt% and subjected to low-velocity impact tests. Emission spectra were collected for each composite before and after impacts across a range of forces. Consistent with the behavior observed in PVAc-based composites, all materials exhibited a distinct MLC response characterized by a red-shift in the emission spectra following impact (Fig. 7a-d). This shift was visually apparent under UV illumination of the impacted areas (Fig. 7e). Moreover, ratiometric plots of I_{Green}/I_{Blue} emission intensity demonstrated a linear correlation with the applied force (Fig. 7f and Table S10). Notably, comparisons across different polymeric matrices revealed that matrices with higher T_g values, such as PC and the epoxy-based resin, exhibited a more pronounced MLC response under impact. In contrast, matrices with lower T_g values, such as PCL and PU, showed a lower response (Table S10). This behavior is likely ascibed to the differing energy dissipation mechanisms of the matrices. In softer matrices, the kinetic energy from impact is dissipated through matrix deformation, reducing the stress transferred to the filler. Conversely, stiffer matrices ensure better energy transfer to the filler, resulting in a stronger MLC response. These findings underscore the critical role of matrix properties in modulating the performance of MLC composites based on this technology.

Conclusions

This study demonstrated the successful development of novel MLC composite materials based on the incorporation of a copper(I) halide hybrid coordination polymer ([(CuI)3-Br-py]$_n$) in various polymer matrices. The synthesized HCP exhibited a fast and sensitive MLC response under impact and shear forces, shifting its emission from blue to green. When incorporated into PVAc, the MLC properties of the filler were successfully transferred to the composite, showing a highly sensitive and reproducible MLC response, shifting its emission color from blue to green upon applying various mechanical stresses, including tensile strain, compression, and impact. Under tensile stress, the composites exhibit a linear correlation between the applied strain and the MLC response for strain below 75 %. Notably, this response was proven to be unaffected by the concentration of the filler and strain-rate dependent, highlighting its potential in applications requiring precise mapping of the mechanical response. The composite showed a remarkable response against compression and impact forces, independent from both the filler concentration and the compression rate. The MLC response in impact tests was found to be linearly correlated to the force applied, over a broad range of forces. Additionally, the composites retained their optical properties over time and after temperature variations, demonstrating excellent stability and persistence of the MLC response. This result, combined with the high sensitivity, addresses a key limitation of current mechanochromic materials, which often suffer from time-dependent responses or require high stresses/strains to trigger any response. Finally, by varying the polymeric matrix, it was possible to prove the versatility of ([(CuI)3-Br-py]$_n$ as mechanoluminochromic filler. The comparative study revealed that the extent of the MLC response is closely tied to the thermal and mechanical characteristics of the matrix. Specifically, matrices with higher T_g values, such as polycarbonate (PC) and epoxy-based coating, exhibited more pronounced MLC shifts compared to softer matrices like polycaprolactone (PCL) and polyurethane (PU). This distinction underscores the role of energy dissipation mechanisms in determining the effectiveness of stress transfer from the matrix to the filler. These findings pave the way for developing novel mechanoluminochromic composites active under different deformation modes and highlight the importance of selecting appropriate matrix materials to optimize the desired mechanoluminochromic response, opening exciting avenues for stress and damage sensing applications, structural health monitoring, and security marking.

Experimental section

Materials

Acetonitrile (MeCN), Dichloromethane (DCM), 3-Bromopyridine (3Br-py), Copper Iodide (CuI), and Acetone were purchased from Merck and used without further purification. Polyvinyl acetate (M_w 500 000 g·mol^{-1}) (PVAc), poly[4,4′-methylenebis(phenyl-isocyanate)-alt-1,4-butanediol/di(propyleneglycol)/poly caprolactone] (PU), Polycaprolactone (M_w 80 000 g·mol^{-1}) (PCL) were purchased from Merck. Polycarbonate (PC) was purchased from Sigma Aldrich. Water-based epoxy resin (Epoxy) was kindly provided by Renner Italia.

Synthesis of [(CuI)3-Br-py]$_n$ powder

In a 10 mL vial, 1 mmol of CuI was suspended in 1 mL of MeCN, and 1.5 mmol of 3Br-py was added (Fig. 2a). The yellow suspension was magnetically stirred at 600 rpm. After 1 h, the slurry color turned white. After 24 h, the reaction was stopped, and to remove any traces of unreacted reagents, the dispersion was transferred to a 15 mL vial with 10 mL of MeCN. The dispersion was centrifuged at 300 rpm for 30 s and left for 1 min to allow the sedimentation of [(CuI)3-Br-py]$_n$ powder. The supernatant, containing the solubilized unreacted reagents, was then removed. This procedure was repeated three times. Residual traces of MeCN were then removed through repeated washings of [(CuI)3-Br-py]$_n$ powder with acetone. A final washing step was then performed with DCM to facilitate residual solvent evaporation. The final product was

obtained as a white powder with a yield of 78 %.

Grinding of [(CuI)3-Br-py]$_n$ pristine powder

200 mg of [(CuI)3-Br-py]$_n$ pristine powder were ground in a Retsch mm200 vibrating ball mill for 5 min at 25 Hz using a 5 mL agata jar and an agata ball with a 7 mm diameter.

Recycling of [(CuI)3-Br-py]$_n$ ground powder

200 mg of [(CuI)3-Br-py]$_n$ pristine powder were ground in a Retsch mm200 vibrating ball mill for 5 min at 25 Hz using a 5 mL agata jar and an agata ball with a 7 mm diameter. This powder was then placed in a 5 mL open vial inserted in a larger 10 mL vial containing 2 mL of MeCN. The 10 mL vial was kept at room temperature for 48 h with the lid on to saturate the environment with MeCN vapors.

Synthesis of [(CuI)3-Br-py]$_n$ single crystals

[(CuI)3-Br-py]$_n$ single crystals were prepared via triple-layer crystallization. The system was prepared by dispensing on the bottom of a test tube 1 mL of a 0.4 M solution of CuI in a $KI_{(aq)}$ saturated solution. On top of the CuI solution, a layer of ethanol (1 mL) was added dropwise as a buffer solvent. Lastly, 1 ml of 3-Br-py solution in acetone (0.4 M) has been added dropwise on top of the ethanol layer. After 24 h, colorless single crystals were obtained at the bottom of the test tube.

Film preparation

PVAc was dissolved in DCM (4 % w/v), and [(CuI)3-Br-py]$_n$ powder was dispersed in DCM (2 % w/v). After 5 min stirring at 600 rpm, the HCP dispersion was added to the polymer solution and cast in a Teflon petri dish. After 48 h, the films were removed from the petri dish and placed in a vacuum oven at 60 °C for 6 h to remove solvent residues. Proper amounts of HCP dispersion were added to the polymer solution to produce composites with a nominal concentration of [(CuI)3-Br-py]$_n$ of 2.5 wt%, 5 wt%, 7.5 wt% and 10 wt%. These composites were labeled 2.5 wt%, 5 wt%, 7.5 wt% and 10 wt%, accordingly.

PC films containing 5 wt% of [(CuI)3-Br-py]$_n$ powder were produced following the above-described procedure. PU films were obtained in the same way, but dissolving the polymer in THF. PCL films were obtained similarly to PU, but the vacuum oven was set at 30 °C. For the preparation of epoxy-based resin, a dispersion of [(CuI)3-Br-py]$_n$ in the prepolymer was prepared. The dispersion was stirred at 600 rpm for 5 min, after which the crosslinking agent was added. The resulting formulation was used to brush-coat carbon fiber-based composites. The composites coated with the mechanoluminochromic coating were cured at 60 °C for 48 h. The resulting coating was produced with a nominal chromophore concentration of 5 wt%.

To produce PVAc films containing [(CuI)3-Br-py]$_n$ single crystals, the solution of PVAc in DCM was added with the dispersion of [(CuI)3-Br-py]$_n$ single crystals and 1 mL of MeCN. The solution was cast and placed in a vacuum oven, as previously described. The obtained film was labelled SC-2 wt%.

Characterization techniques

Single-crystal X-ray diffraction data at room temperature were collected with an Oxford Diffraction X'Calibur S CCD diffractometer equipped with a graphite monochromator and a CCD detector. Mo − Kα radiation ($\lambda = 0.71073$ Å) was used. A single crystal of [(CuI)3-Br-py]$_n$ was selected and mounted on the diffractometer; the crystal was kept at 293(2) K during data collection. Using Olex2,[60] the structure was solved with the SHELXT[61] by Intrinsic Phasing and refined on F^2 with SHELXL[62] refinement package, by full matrix least squares refinement. H_{CH} atoms were added in calculated positions and refined riding on their respective carbon atoms. All non-hydrogen atoms were refined anisotropically. The program Mercury[63] was used for graphic representations. Crystal data and refinement details are listed in Table S1. Crystallographic data for the structures reported in this paper have been deposited in the Cambridge Crystallographic Data Centre as supplementary publication No. CCDC 2466496.

X-ray diffraction patterns of powder samples for WPPM analysis were collected in Bragg–Brentano geometry on a PANalytical Empyrean automated diffractometer using Cu–Kα radiation ($\lambda = 1.5418$ Å) without a monochromator in the 5 – 80° 2θ range. The instrument, operating at 40 kV/40 mA, is equipped with Bragg Bentano HD optics. A PIXcel3D area detector with 255 active channels with ~3° 2θ of coverage was used for data collection (continuous scan mode, step size 0.0131°; counting time 68.595 s; incident beam soller slit 0.03 rad, diffracted beam soller slit 0.02 rad, divergence slit (incident beam) 0.25, anti-scatter slit (diffracted beam) 0.25.

Microstructural analysis was carried out through diffraction line profile modelling using TOPAS-Academic Version 7 and the Whole Powder Pattern Modelling (WPPM) approach. WPPM employs a fundamental parameter-based description of the microstructure to generate theoretical line profiles. Within this approach, the observed line profile is the result of the convolution of various contributions: instrumental broadening, coherent domain size and shape, and lattice distortions. Microstructural parameters are extracted via Rietveld refinement (non-linear least squares fitting) of the experimental pattern. In this work, WPPM was employed under the assumption that sample-induced broadening arises exclusively from variations in coherent domain size, with contributions from lattice strain and anisotropic effects considered negligible. This modelling strategy, previously applied with molecular materials [64], enables the tracking of microstructural evolution across recycling cycles by focusing on changes in domain size distribution. Crystallites were modelled as equiaxed spherical domains with a lognormal distribution of diameters, described by the parameters μ and σ, obtained via Rietveld refinement (Figs. S4 and S11, Tables S2 and S3).

X-ray diffraction patterns of polymeric films were collected on a PANalytical X'Pert Pro automated diffractometer equipped with an X'celerator detector in Bragg–Brentano geometry using Cu–Kα radiation ($\lambda = 1.5418$ Å) without monochromator in the 5 Xr– 80° 2θ range (step size 0.033°; time/step: 20 s; Soller slit 0.04 rad, anti-scatter slit: 1/2, divergence slit: 1/4; 40 mA•40 kV).

Images under white light and UV light were collected exploiting a Canon EOS 1000D equipped with an 18–55 mm lens and a band-pass filter at 400 nm.

[(CuI)3-Br-py]$_n$ morphology was investigated by SEM analysis using a Zeiss LEO 1530 FE-SEM operated at 5 kV. Samples were gold sputtered before the analysis. Average crystal length and diameter were determined by exploiting ImageJ analysis software (NIH, USA) after measuring 150 crystals, and the results are given as the center of the lognormal distribution ± standard deviation (SD).

Emission spectra in the solid state were acquired by exploiting a Thorlabs compact spectrometer (CCS200M, optical fiber with a 200 μm apical aperture) coupled with a 365 nm LED (ThorLabs SOLIS-365c) as the near-field probe.

Mechanoluminochromic grinding tests were conducted using a homemade setup composed of a stepper motor connected to a 3D-printed rotating plate placed on top of a glass petri dish. 100–200 mg of powder sample were tested employing a 6 rad·s^{-1} rotation speed, and their emission spectra were acquired at 2 Hz frequency by using the Thorlabs compact spectrometer coupled with the 365 nm LED. A video of the experiment was recorded using a 45° mirror placed under the rotating plate. A schematic representation of the setup employed is reported in Fig. S6.

Confocal microscopy images were collected using a Nikon A1R confocal microscope system with 20x and 40x magnification, numerical aperture, NA, respectively of 0.75 and 0.95 of Nikon Plan-Apo objective

lens. The samples were excited by a continuous wave laser at 405 nm. The emission of the films was collected at 450 ± 25 nm and 525 ± 25 nm.

Thermogravimetric analysis (TGA) was performed using a Q500 TGA thermogravimetric analyzer (TA Instruments). All the analyses were performed on 5–6 mg samples placed in a platinum pan. The heating ramp was performed from room temperature to 600 °C at a heating rate of 10 °C·min^{-1} under nitrogen flow.

Differential Scanning Calorimetry (DSC) was carried out using a Q2000 DSC apparatus (TA instruments) equipped with a Refrigerated Cooling System (RCS90). The analyses were performed on 4–6 mg samples placed inside aluminum pans under nitrogen flow. The samples under analysis were subjected to two heating scans at a rate of 20 °C·min^{-1} alternated with a fast cooling (quenching).

Polarized optical microscope (POM) images and videos were collected using a Zeiss Axioscope microscope equipped with a Zeiss Axiocam 208 color and analyzed with Zen 3.6 software. Samples were tested in tensile mode under the POM using a Linkam MFS stage equipped with the LINK software package. Dog-bone-shaped samples were prepared following ASTM D1708 (gauge length = 14 mm, width = 5 mm, thickness = 0.2–0.3 mm) and were tested in traction mode with a load cell of 200 N. The crosshead speed was set at 2.4 %·s^{-1}. Crystal orientation with respect to the strain direction was determined by measuring the orientation of 150 crystals using ImageJ analysis software (NIH, USA). The results are given as the average orientation with respect to the elongation direction ± standard deviation (SD).

Stress–strain tests were conducted using an Instron Testing Machine 4465 equipped with the Bluehill universal software package. Dog-bone-shaped samples were prepared following ASTM D1708 (gauge length = 14 mm, width = 5 mm, thickness = 0.2–0.3 mm) and were tested in traction mode with a load cell of 100 N. The crosshead speed was set at either 2.4 %·s^{-1} or 24 %·s^{-1}. For each material, at least 3 samples of each type were tested. During stress–strain tests, emission spectra were acquired at 2 Hz frequency by using the Thorlabs compact spectrometer coupled with the 365 nm LED. A schematic representation of the setup is reported in Fig. 4a.

Compression tests were conducted using a Instron 8033 servo-hydraulic testing machine, equipped with a 25 kN load cell. Rectangular-shaped samples (length = 20 mm, width = 20 mm, thickness = 0.2–0.5 mm) were compressed between a glass fiber reinforced plate 6 mm thick and a steel indenter with a 12.7 mm hemispherical steel tip (same indenter shape employed in the low velocity impact test). Load was applied between 0 to −1500 N, in force control mode with a half-sinusoidal shape to mimic an elastic impact, at different rates: 0.08, 0.6 and 4.3 N·ms^{-1}. For each MLC concentration and compression rate 3 specimens were tested. A schematic representation of the setup is reported in Fig. S19. Emission spectra of the compressed sample were then acquired by using the Thorlabs compact spectrometer coupled with the 365 nm LED. At least 10 spectra of the compressed area were recorded and then averaged exploiting the "acquire and average" feature embedded in the ThorSpectra software used for the acquisition.

Low-velocity impact tests were performed according to ASTM D7136 standard using a drop-weight tower with a 1.3 kg impactor mass equipped with a PCB 208C05 load cell and 12.7 mm hemispherical steel tip (note same geometry of the compression test indenter). The samples were placed on top of the same glass-fiber reinforced plate employed for the compression test. Tests were conducted at different nominal maximum impact forces of 500, 1000, 1500, 2000, and 2800 N by adjusting the impact height. For each MLC concentration and impact force, 3 samples of each type were tested.

The same setup was also employed to test [(CuI)3-Br-py]$_n$ based composite having other polymeric matrices, in this case 3 nominal forces were chosen (1500, 2500, and 3100 N). A schematic representation of the setup is reported in Fig. S21.

Emission spectra of both compressed and impacted sample were acquired by using the Thorlabs compact spectrometer coupled with the 365 nm LED. At least 10 spectra of the indented area were recorded and then averaged exploiting the "acquire and average" feature embedded in the ThorSpectra software used for the acquisition.

Funding sources

This work was financially supported by the European Union – NextGenerationEU under the National Recovery and Resilience Plan (PNRR) – Mission 4 Education and research, from "Piezochromic smart auto-diagnostic polymer coatings – STIGMA", proposal code P20223WB9K – CUP J53D23014670001, by AlmaIdea 2022 project supported by the University of Bologna, and by a SPS NATO grant (project number G6238) "a new Chromogenic technOLOgy foR on-field Damage detectiOn – COLORaDO". The authors acknowledge Dr. L. Benni and Dr. M. Soverini from Renner Italia for providing coating formulations.

CRediT authorship contribution statement

E. Contini: Writing – original draft, Visualization, Methodology, Investigation, Formal analysis, Data curation, Conceptualization. **L. Contini:** Writing – original draft, Visualization, Methodology, Investigation, Formal analysis, Data curation, Conceptualization. **L. Gatti:** Writing – review & editing, Investigation, Formal analysis, Data curation. **F. Mongioì:** Writing – review & editing, Methodology, Investigation, Formal analysis. **D. Fazzi:** Writing – review & editing, Methodology, Investigation. **T.M. Brugo:** Writing – review & editing, Supervision, Resources, Methodology, Conceptualization. **D. Genovese:** Writing – review & editing, Supervision, Resources, Methodology, Funding acquisition, Data curation, Conceptualization. **L. Maini:** Writing – review & editing, Supervision, Resources, Methodology, Funding acquisition, Data curation, Conceptualization. **C. Gualandi:** Writing – review & editing, Supervision, Resources, Methodology, Funding acquisition, Conceptualization.

Declaration of competing interest

The authors declare that they have no known competing financial interests or personal relationships that could have appeared to influence the work reported in this paper.

Appendix A. Supplementary data

Supplementary data to this article can be found online at https://doi.org/10.1016/j.mattod.2025.11.034.

Data availability

Data will be made available on request.

References

[1] Y. Chen, M. Sommer, C. Weder, Mechanochromic polymers, Macromol. Rapid Commun. 42 (2021) 1–3, https://doi.org/10.1002/marc.202000685.
[2] A. Pucci, G. Ruggeri, Mechanochromic polymer blends, J. Mater. Chem. 21 (2011) 8282–8291, https://doi.org/10.1039/c0jm03653f.
[3] C. Calvino, et al., Approaches to polymeric mechanochromic materials, J. Polym. Sci. A Polym. Chem. 55 (2017) 640–652, https://doi.org/10.1002/pola.28445.
[4] C. Micheletti, et al., Blending or bonding? Mechanochromism of an aggregachromic mechanophore in a thermoplastic elastomer, ACS Appl. Polym. Mater. 5 (2023) 1545–1555, https://doi.org/10.1021/acsapm.2c02037.
[5] E. Contini, et al., Comparative mechanochromic performance of perylene diimide-doped polyurethanes: Blending vs bonding, ACS Appl. Polym. Mater. 6 (2024) 669–680, https://doi.org/10.1021/acsapm.3c02284.
[6] C. Micheletti, et al., Mechanochromic LLDPE Films doped with NIR reflective paliogen black, Macromol. Rapid Commun. 42 (2021), https://doi.org/10.1002/marc.202000426.
[7] F. Cellini, et al., Large deformations and fluorescence response of mechanochromic polyurethane sensors, Mech. Mater. 93 (2016) 145–162, https://doi.org/10.1016/j.mechmat.2015.10.013.

[8] B.R. Crenshaw, et al., Deformation-induced color changes in mechanochromic polyethylene blends, Macromolecules 40 (2007) 2400–2408, https://doi.org/10.1021/ma062936j.

[9] Y. Sagara, et al., Temperature-dependent mechanochromic behavior of mechanoresponsive luminescent compounds, Chem. Mater. 29 (2017) 1273–1278, https://doi.org/10.1021/acs.chemmater.6b04720.

[10] F. Ciardelli, G. Ruggeri, A. Pucci, Dye-containing polymers: Methods for preparation of mechanochromic materials, Chem. Soc. Rev. 42 (2013) 857–870, https://doi.org/10.1039/c2cs35414d.

[11] C. Löwe, C. Weder, Oligo(p-phenylene vinylene) excimers as molecular probes: Deformation-induced color changes in photoluminescent polymer blends, Adv. Mater. 14 (2002) 1625–1629, https://doi.org/10.1002/1521-4095(20021118)14:22<1625::AID-ADMA1625>3.0.CO;2-Q.

[12] B.R. Crenshaw, C. Weder, Self-assessing photoluminescent polyurethanes, Macromolecules 39 (2006) 9581–9589, https://doi.org/10.1021/ma061685b.

[13] B.R. Crenshaw, C. Weder, Deformation-induced color changes in melt-processed photoluminescent polymer blends, Chem. Mater. 15 (2003) 4717–4724, https://doi.org/10.1021/cm034447t.

[14] H. Traeger, et al., From molecules to polymers—Harnessing inter- and intramolecular interactions to create mechanochromic materials, Macromol. Rapid Commun. 42 (2021) 1–32, https://doi.org/10.1002/marc.202000573.

[15] Y. Zhuang, et al., Mechanoluminescence rebrightening the prospects of stress sensing: A review, Adv. Mater. 33 (2021) 2005925, https://doi.org/10.1002/ADMA.202005925.

[16] J.C. Zhang, et al., Trap-controlled mechanoluminescent materials, Prog. Mater Sci. 103 (2019) 678–742, https://doi.org/10.1016/J.PMATSCI.2019.02.001.

[17] L. Metzler, et al., High molecular weight mechanochromic spiropyran main chain copolymers via reproducible microwave-assisted Suzuki polycondensation, Polym. Chem. 6 (2015) 3694–3707, https://doi.org/10.1039/c5py00141b.

[18] C.K. Lee, et al., Exploiting force sensitive spiropyrans as molecular level probes, Macromolecules 46 (2013) 3746–3752, https://doi.org/10.1021/ma4005428.

[19] M. Sommer, Substituent effects control spiropyran–merocyanine equilibria and mechanochromic utility, Macromol. Rapid Commun. 42 (2021) 1–9, https://doi.org/10.1002/marc.202000597.

[20] H. Traeger, et al., Folded perylene diimide loops as mechanoresponsive motifs, Angew. Chem. 133 (2021) 16327–16335, https://doi.org/10.1002/ange.202105219.

[21] H. Traeger, et al., Strain-correlated mechanochromism in different polyurethanes featuring a supramolecular mechanophore, Polym. Chem. 13 (2022) 2860–2869, https://doi.org/10.1039/D2PY00218C.

[22] C. Weder, mechanochromic polymers, encyclopedia of polymeric, Nanomaterials (2013) 1–11, https://doi.org/10.1007/978-3-642-36199-9_6-4.

[23] N. Deneke, M.L. Rencheck, C.S. Davis, An engineer's introduction to mechanophores, Soft Matter 16 (2020) 6230–6252, https://doi.org/10.1039/D0SM00465K.

[24] V.A. Dini, et al., In situ monitoring of mechanofluorescence in polymeric nanofibers, Macromol. Rapid Commun. (2024) 2400855, https://doi.org/10.1002/MARC.202400855.

[25] J. Liu, et al., Perylene diimide-based supramolecular polymer with temperature-sensitive ratiometric fluorescence responsiveness in solution and gels, Mater. Adv. 1 (2020) 1330–1336, https://doi.org/10.1039/D0MA00053A.

[26] A. Pucci, et al., Bis(benzoxazolyl)stilbene excimers as temperature and deformation sensors for biodegradable poly(1,4-butylene succinate) films, J. Mater. Chem. 17 (2007) 783–790, https://doi.org/10.1039/B612033D.

[27] B. Poggi, et al., Mechanofluorochromic difluoroboron β-diketonates based polymer composites: Toward multi-stimuli responsive mechanical stress probes, Macromol. Rapid Commun. 43 (2022) 2200134, https://doi.org/10.1002/MARC.202200134.

[28] T. Yamamoto, A. Takahashi, H. Otsuka, Mechanochromic polymers based on radical-type dynamic covalent chemistry, Bull. Chem. Soc. Jpn 97 (2024), https://doi.org/10.1093/BULCSJ/UOAD004.

[29] Y. Chen, et al., Mechanochemical tools for polymer materials, Chem. Soc. Rev. 50 (2021) 4100–4140, https://doi.org/10.1039/D0CS00940G.

[30] D.R.T. Roberts, S.J. Holder, Mechanochromic systems for the detection of stress, strain and deformation in polymeric materials, J. Mater. Chem. 21 (2011) 8256–8268, https://doi.org/10.1039/C0JM04237D.

[31] K. Imato, et al., Repeatable mechanochemical activation of dynamic covalent bonds in thermoplastic elastomers, Chem. Commun. 52 (2016) 10482–10485, https://doi.org/10.1039/C6CC04767J.

[32] D. Kim, M.S. Kwon, C.W. Lee, Mechanochromic polymers with a multimodal chromic transition: Mechanophore design and transduction mechanism, Polym. Chem. 13 (2022) 5177–5187, https://doi.org/10.1039/D2PY00435F.

[33] J. Conesa-Egea, F. Zamora, P. Amo-Ochoa, Perspectives of the smart Cu-Iodine coordination polymers: A portage to the world of new nanomaterials and composites, Coord. Chem. Rev. 381 (2019) 65–78, https://doi.org/10.1016/J.CCR.2018.11.008.

[34] M.J. Leitl, et al., Copper(I) complexes for thermally activated delayed fluorescence: From photophysical to device properties, Top. Curr. Chem. 374 (2016), https://doi.org/10.1007/s41061-016-0019-1.

[35] E. Cariati, et al., Cu(I) hybrid inorganic-organic materials with intriguing stimuli responsive and optoelectronic properties, Coord. Chem. Rev. 306 (2016) 566–614, https://doi.org/10.1016/j.ccr.2015.03.004.

[36] M. Vitale, W.E. Palke, P.C. Ford, Origins of the double emission of the tetranuclear copper(I) cluster Cu4I4(pyridine)4: An ab initio study, J. Phys. Chem. 96 (1992) 8329–8336, https://doi.org/10.1021/j100200a023.

[37] S. Perruchas, Molecular copper iodide clusters: A distinguishing family of mechanochromic luminescent compounds, Dalton Trans. 50 (2021) 12031–12044, https://doi.org/10.1039/D1DT01827B.

[38] Y. Song, et al., Copper(I)-iodide based coordination polymers: Bifunctional properties related to thermochromism and PMMA-doped polymer film materials, J. Mater. Chem. C Mater. 3 (2015) 6249–6259, https://doi.org/10.1039/c5tc01273b.

[39] J.C. Egea, Materials and nanomaterials with stimuli-responsive behaviour based on the flexibility of the copper-halide by, (2019).

[40] J. Troyano, et al., Reversible thermochromic polymeric thin films made of ultrathin 2D crystals of coordination polymers based on copper(I)-thiophenolates, Adv. Funct. Mater. 28 (2018) 1704040, https://doi.org/10.1002/ADFM.201704040.

[41] J. Conesa-Egea, et al., Smart composite films of nanometric thickness based on copper–iodine coordination polymers, Toward Sensors, Chem. Sci. 9 (2018) 8000–8010, https://doi.org/10.1039/C8SC03085E.

[42] Q. Benito, et al., Mechanochromic luminescence of copper iodide clusters, Chem. – A Europ. J. 21 (2015) 5892–5897, https://doi.org/10.1002/CHEM.201500251.

[43] C. Cappuccino, et al., Mechanochemistry, an easy technique to boost the synthesis of cui pyrazine coordination polymers, Cryst. Growth Des. 19 (2019) 4395–4403, https://doi.org/10.1021/ACS.CGD.9B00192/ASSET/IMAGES/LARGE/CG-2019-001926_0008.JPEG.

[44] L. Maini, et al., Mechanochemical preparation of copper iodide clusters of interest for luminescent devices, Faraday Discuss. 170 (2014) 93–107, https://doi.org/10.1039/c3fd00164d.

[45] D. Braga, et al., Solid-state reactivity of copper(i) iodide: Luminescent 2D-coordination polymers of CuI with saturated bidentate nitrogen bases, New J. Chem. 35 (2011) 339–344, https://doi.org/10.1039/c0nj00547a.

[46] F. Farinella, et al., White luminescence achieved by a multiple thermochromic emission in a hybrid organic-inorganic compound based on 3-picolylamine and copper(i) iodide, Dalton Trans. 45 (2016) 17939–17947, https://doi.org/10.1039/c6dt03049a.

[47] M. Murillo, et al., 2D Cu(I)-I coordination polymer with smart optoelectronic properties and photocatalytic activity as a versatile multifunctional material, Inorg. Chem. 62 (2023) 10928–10939, https://doi.org/10.1021/ACS.INORGCHEM.3C00616/ASSET/IMAGES/LARGE/IC3C00616_0012.JPEG.

[48] A. Vogler, H. Kunkely, Photoluminescence of tetrameric copper(I) iodide complexes in solution, J. Am. Chem. Soc. 108 (1986) 7211–7212, https://doi.org/10.1021/JA00283A012/ASSET/JA00283A012.FP.PNG_V03.

[49] D. Tran, J.L. Bourassa, P.C. Ford, Pressure-induced luminescence rigidochromism in the photophysics of the cuprous iodide cluster Cu4I4py4, Inorg. Chem. 36 (1997) 439–442, https://doi.org/10.1021/IC960959G/ASSET/IMAGES/LARGE/IC960959GF00003.JPEG.

[50] E. Cariati, X. Bu, P.C. Ford, Solvent- and vapor-induced isomerization between the luminescent solids [CuI(4-pic)]4 and [CuI(4-pic)]∞ (pic = methylpyridine) the structural basis for the observed luminescence vapochromism, Chem. Mater. 12 (2000) 3385–3391, https://doi.org/10.1021/CM0010708.

[51] S. Masahara, et al., Convenient synthesis of copper(I) halide quasi-one-dimensional coordination polymers: Their structures and solid-state luminescent properties, Dalton Trans. 50 (2021) 8889–8898, https://doi.org/10.1039/D1DT01571K.

[52] N.V.S. Harisomayajula, S. Makovetskyi, Y.C. Tsai, Cuprophilic Interactions in and between molecular entities, Chem. – A Europ. J. 25 (2019) 8936–8954, https://doi.org/10.1002/CHEM.201900332.

[53] X. Zhang, et al., Systematic approach in designing rare-earth-free hybrid semiconductor phosphors for general lighting applications, J. Am. Chem. Soc. 136 (2014) 14230–14236, https://doi.org/10.1021/JA507927A/SUPPL_FILE/JA507927A_SI_001.PDF.

[54] P. Scardi, Diffraction line profiles in the rietveld method, Cryst. Growth Des. 20 (2020) 6903–6916, https://doi.org/10.1021/ACS.CGD.0C00956/ASSET/IMAGES/LARGE/CG0C00956_0008.JPEG.

[55] A. Aguirrechu-Comerón, et al., Experimental and ab Initio Study of Catena(bis(μ2-iodo)-6-methylquinoline-copper(I)) under pressure: Synthesis, crystal structure, electronic, and luminescence properties, Inorg. Chem. 55 (2016) 7476–7484, https://doi.org/10.1021/acs.inorgchem.6b00796.

[56] B.A. Alshammari, et al., Comprehensive review of the properties and modifications of carbon fiber-reinforced thermoplastic composites, Polymers (basel) 13 (2021), https://doi.org/10.3390/polym13152474.

[57] S.K. Singh, A. Kumar, A. Jain, Effect of nanoparticles dispersion on viscoelastic properties of epoxy-zirconia polymer nanocomposites, in: IOP Conf Ser Mater Sci Eng, Institute of Physics Publishing, 2018, https://doi.org/10.1088/1757-899X/330/1/012001.

[58] F. Rezaei, R. Yunus, N.A. Ibrahim, Effect of fiber length on thermomechanical properties of short carbon fiber reinforced polypropylene composites, Mater. Des. 30 (2009) 260–263, https://doi.org/10.1016/j.matdes.2008.05.005.

[59] P.J. Centellas, K.D. Mehringer, A.L. Bowman, K.M. Evans, P. Vagholkar, T. L. Thornell, L. Huang, S.E. Morgan, C.L. Soles, Y.C. Simon, E.P. Chan, Mechanochemically responsive polymer enables shockwave visualization, Nat. Commun. 15 (2024) 1–10, https://doi.org/10.1038/s41467-024-52663-1.

[60] O. V. Dolomanov, L.J. Bourhis, R.J. Gildea, J.A.K. Howard, H. Puschmann, OLEX2: a complete structure solution, refinement and analysis program, Urn:Issn:0021-8898 42 (2009) 339–341. https://doi.org/10.1107/S0021889808042726.

[61] G.M. Sheldrick, SHELXT – Integrated space-group and crystal-structure determination, Urn:Issn:2053-2733, 71 (2015) 3–8. https://doi.org/10.1107/S2053273314026370.

[62] G.M. Sheldrick, Crystal structure refinement with SHELXL, Urn:Issn:2053-2296, 71 (2015) 3–8. https://doi.org/10.1107/S2053229614024218.
[63] C.F. Macrae, I.J. Bruno, J.A. Chisholm, P.R. Edgington, P. McCabe, E. Pidcock, L. Rodriguez-Monge, R. Taylor, J. Van De Streek, P.A. Wood, Mercury CSD 2.0 – new features for the visualization and investigation of crystal structures, Urn:Issn: 0021–8898 41 (2008) 466–470, https://doi.org/10.1107/S0021889807067908.
[64] C. Fandaruff, et al., Correlation between microstructure and bioequivalence in Anti-HIV Drug Efavirenz, Eur. J. Pharm. Biopharm. 91 (2015) 52–58, https://doi.org/10.1016/J.EJPB.2015.01.020.